Check for updates

Electrocatalytic methanol oxidation with nanoporous gold: microstructure and selectivity†

Matthias Graf, [ID] *[a] Mareike Haensch, [ID] [b] Jörg Carstens, [ID] [c] Gunther Wittstock [ID] [b] and Jörg Weissmüller [ID] [a,d]

The properties of Nanoporous Gold (NPG) obtained by the selective dissolution of Ag from an Au–Ag alloy can be tuned by the details of its fabrication, and specifically the residual Ag content is correlated to the ligament size of the material. We link this correlation to methanol electro-oxidation. Specifically, two different NPG types (obtained by potentiostatic dealloying) are compared with one obtained by free corrosion. They show remarkable differences in activity. Quantitative product analysis reveals that NPG shows nearly selective oxidation of CH_3OH to $HCOO^-$ when NPG is used as an active electrode in contrast to planar Au. This trend can further be enhanced when applying finer nanoporous structures that are linked to a higher Ag content. X-ray photoelectron spectroscopy (XPS) reveals changes in the nature of residual Ag from which we conclude that Ag is not a passive component in the methanol oxidation process.

1 Introduction

Nanoporous gold (NPG) has been investigated for (and applied in) a large variety of applications within the past two decades. Amongst its use as a sensor/actuator,[1–4] optically tunable[5] or energy storage[6] material, especially its use as a catalyst[7,8] was investigated.

NPG is currently regarded as a promising Pt-free alternative catalyst material.[9] Bulk-NPG is produced by 'dealloying', *i.e.* the selective etching of a sacrificial metal (Ag,[10] Cu[11] or Al[12]) from a homogeneous Au alloy. The resulting structure consists of an open porous network of 10–60 nm struts or 'ligaments'. The catalytic activity as well as selectivity of NPG towards catalytic gas[7] or liquid phase[13] reactions has been demonstrated to be remarkably higher than for planar Au.[14] Dealloying-induced strain,[15,16] the high density of surface defects and atomic step edges at the ligament surface[17] accompanied by traces of the sacrificial metal Ag[18] were identified as reasons creating a chemical activity high enough to promote the dissociation of molecular oxygen.[19]

Some time ago Zhang *et al.*[20] investigated the electrocatalytic conversion of methanol using NPG electrodes of a few micrometers thick and extended the evidence of high catalytic activity to heterogeneous electrocatalysis. Methanol electro-oxidation (MEO) was once considered the most important candidate for the anodic partial reaction in fuel cells due to the high energy density of methanol besides its low price and hazardousness; yet formaldehyde formation is considered critical. The most common electrocatalyst materials are composed of Pt[21] or Pt–Ru[22] nanoparticles that are dispersed over a (porous) carbon carrier. Pt-based catalysts suffer from poisoning by CO as well as high cost. NPG-based catalysts were not found to show such drawbacks. Instead, Zhang *et al.*[20] concluded a decrease of the porosity upon electrochemical cycling as the major disadvantage of NPG. Two important points motivate a re-examination of these results: (i) The conclusion of the six-electron reaction product carbonate (CO_3^{2-}) was based on assumptions for planar electrodes[23] during ethanol oxidation[24] and was not supported by experimental evidence. Additionally, long transport paths in NPG as well as the higher activity might substantially influence the product formation paths. (ii) The performance of NPG as an electrocatalyst compared to other porous gold materials with different activities[25–28] is yet unknown. Findings after the publication of ref. 20 suggested that NPG properties vary with the particular dealloying techniques[29] (especially with respect to the surface structure of bulk-NPG[30] or surface-located Ag clusters[31]).

In order to achieve a typological variation of NPG we utilize three different dealloying routes, namely mild and harsh

[a] *Institute of Materials Physics and Technology, Hamburg University of Technology, Hamburg, Germany. E-mail: matthias.graf@tuhh.de; Fax: +49 (0)40 42878 4070; Tel: +49 (0)40 42878 2276*

[b] *Carl von Ossietzky University of Oldenburg, Institute of Chemistry, Oldenburg, Germany*

[c] *Hamburg University of Technology, Central Laboratory for Analytical Chemistry, Hamburg, Germany*

[d] *Institute of Materials Research, Materials Mechanics, Helmholtz-Zentrum Geesthacht, Geesthacht, Germany*
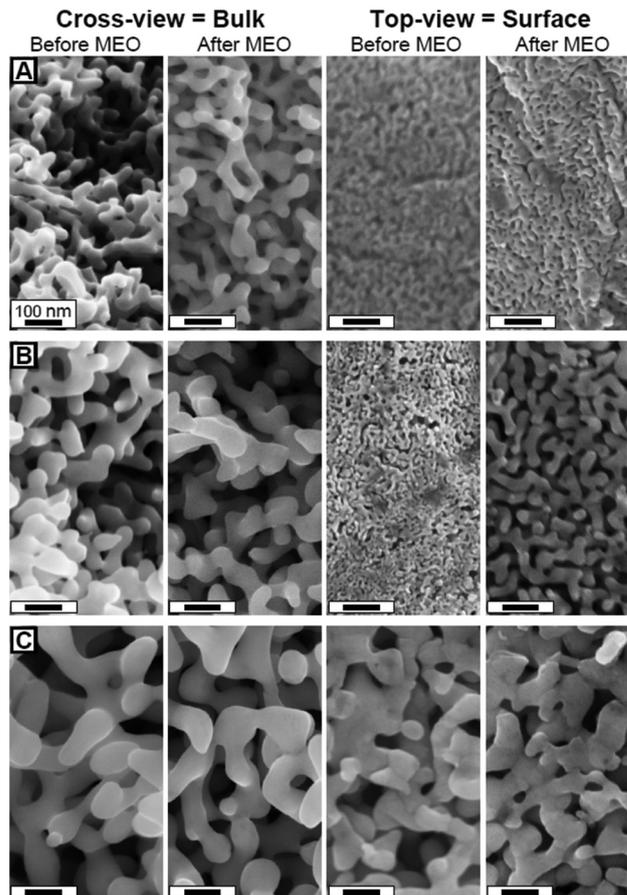
potentiostatic dealloying as well as open-circuit corrosion to generate NPG from an Au–Ag alloy. The determination of the electrochemically active surface area (A) allows comparing MEO signals at different porous electrodes with a planar Au electrode. Chronoamperometric (CA) measurements are performed to assess the long-term activity (*i.e.* the current for methanol oxidation I divided by A) and current efficiency *i.e.* the current for methanol oxidation I divided by the external (geometric) surface area (A_{geom}) of NPG. X-ray photoelectron spectroscopy (XPS) is utilized in order to characterize the nature of Ag present in NPG before and after cyclic voltammetry as well as its influence on the MEO process. Quantitative determination of formaldehyde (HCHO) and formate (HCOO$^-$) contents in the electrolyte after MEO at different electrodes by high-pressure liquid chromatography (HPLC) and ion-exchange chromatography (IEC), respectively, enable conclusions on the selectivity of the reaction. Correlations between the observed electrochemical behavior and the NPG structure, composition and its evolution reveal new insights into the role that Ag and Ag$_2$O play during electrocatalysis.

2   Results and discussion

2.1   Electrode characterization before MEO

Fig. 1 collects scanning electron microscopy (SEM) images of the NPG structures from the different dealloying protocols. All properties as obtained by SEM, energy-dispersive X-ray spectroscopy (EDX), XPS and A determination are listed in Table 1. Ligament sizes in the bulk (L_B) increase from NPG-A to NPG-C. Dealloying routes A and B further result in NPG with a ligament size difference between L_B compared to top-view micrographs that give a surface ligament size, L_S (third row in Fig. 1A). This difference is largest for NPG-B. Both ligament sizes were determined with a single standard error of 10%. EDX was measured in the center of the sample's cross-section, *i.e.* the derived residual Ag contents (x_{Ag}) are considered the bulk Ag concentration. EDX determines a lower x_{Ag} than XPS. EDX values scale in the order NPG-A > NPG-C > NPG-B ≈ 0 while XPS gives NPG-B > NPG-A > NPG-C. The EDX results were verified by additional measurements of the volume-averaged Ag contents by inductively coupled plasma optical emission spectroscopy (ICP-OES, see the ESI†). These show the same trend as those obtained with EDX, although x_{Ag} values are higher due to the compositional heterogeneity.

The active electrode area A was determined using the capacitance ratio method (see Section 1).[32] This method has the advantage that the surface is not modified as would be the case when using a sorption method or procedures based on the underpotential deposition of metals. The capacitance ratio method has been applied to gold before[32,33] and is known to give the most reliable results.[34] Values for A can be found in Table 1. The specific surface area A_m was determined by dividing A by the mass m = 17 mg as determined by weighing a cleaned and dried sample after the dealloying process. We find that A_m is slightly smaller than the literature data[35] for

Fig. 1   Scanning electron micrographs of NPG samples prepared by A: potentiostatic dealloying in HClO$_4$, B: potentiostatic dealloying in HNO$_3$ and by C: open-circuit dealloying in HNO$_3$. Left two columns: cross-sections after sample cleavage. Right two columns: top-views onto the flat sample surface. Cross-views and top-views refer to the state after dealloying (first and third column) and after ten cyclic voltammetry scans in 1 M KOH + 1 M CH$_3$OH (second and fourth column). All scale bars: 100 nm.

the smallest ligaments while matching predictions of theoretical assumptions.[36] For un-cleaved samples (as used for CA measurements) A_{geom} is 0.42 cm^2.

The characteristics of NPG electrodes that were synthesized by different dealloying routes essentially agree with past conclusions on relationships between geometry and composition.[29,37] We find increasing L_B with decreasing x_{Ag} (from EDX) when dealloying proceeds faster (NPG-A *vs.* NPG-B) and further ligament coarsening caused by the elevated temperature during free corrosion (NPG-C). Upon the inspection of A values we find that structures with finer ligaments are connected to a higher A. The measured values for A are in good accordance with the values as derived from a cylinder with a diameter L_B.

Furthermore, for samples originating from potentiostatic dealloying we confirm the presence of a skin layer of ≈100 nm thickness that consists of finer ligaments than the bulk and that covers the outside of the sample. Note, that all samples
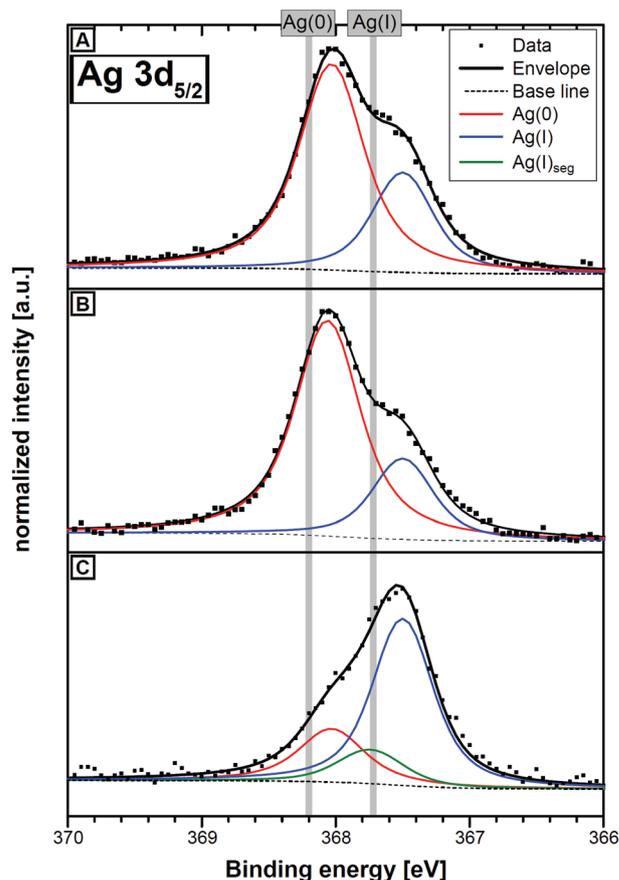
Table 1 Properties of the used NPG and planar Au electrodes: L_B, bulk ligament size; L_S, surface ligament size; x_{Ag}, bulk Ag content as measured by energy-dispersive X-ray diffraction (EDX, bulk) or X-ray photoelectron spectroscopy (XPS, surface); C, electrode capacitance; A, electrochemical active surface area; A_m, mass-specific A; I_P, peak current and E_P, potential of first methanol oxidation peak (AM1, see Fig. 4 and 5) during cyclic methanol electro-oxidation in the first and the tenth cyclic voltammetry (CV) scan in 1 M KOH + 1 M CH$_3$OH; c_{HCHO}, formaldehyde and c_{HCOO^-}, formate concentration in the electrolyte after ten repetitive CV scans. Numbers in italics refer to the respective values after ten CV scans

	NPG-A	NPG-B	NPG-C	Au
L_B [nm]	28	51	69	—
	34	*46*	*67*	—
L_S [nm]	8	9	58	—
	16	*26*	*58*	—
$x_{Ag\text{-}EDX}$ [at%]	3.6	0.1	0.8	—
	4.7	*0.2*	*0.3*	—
$x_{Ag\text{-}XPS}$ [at%]	15.0	16.1	6.7	—
	14.4	*9.1*	*7.2*	—
C [mF]	48.6	32.2	6.4	0.2
A [cm^2]	1216.2	805.0	161.0	5.2
A_m [m^2 g^{-1}]	7.2	4.7	1.0	0.003
I_P/A [μA cm^{-2}]	(1st) 42.0	101.1	119.4	73.8
	(*10th*) *38.4*	*92.3*	*109.8*	—
E_P [mV]	(1st) 550	532	420	280
	(*10th*) *504*	*507*	*403*	*280*
c_{HCHO} [μM]	75.2	303.4	87.9	236.4
c_{HCOO^-} [μM]	2613.0	4095.9	938.4	1288.3

Fig. 2 Normalized XPS Ag 3d$_{5/2}$ core level spectra of the surface of NPG as prepared by the dealloying protocols A–C. Spectra refer to samples NPG-A (A), NPG-B (B) and NPG-C (C). Envelope functions (thick lines), components (thin lines) and background (thin dashed lines) are plotted. The theoretical binding energy of pure Ag is indicated by the grey left vertical line, the one of Ag$_2$O by the right line. Deconvoluted peaks denoted as "Ag(0)" (red line) are assigned to Ag(0) alloyed with Au (Ag$_{50}$Au$_{50}$), peaks at 367.5 eV to Ag(I) (blue line) and the "Ag(I)$_{seg}$" peak in C (green line) is assigned to Ag(I) in higher concentration.

were made from one alloy ingot that was homogenized intensively before cold-rolling so that the skin cannot be caused by Ag concentration gradients. Besides a more detailed explanation for this observation, our previous studies have established a correlation between residual silver content and ligament size.[29,31] According to this observation, the skin with smaller ligaments must have a higher Ag content than the bulk of a NPG sample.

For a binding energy (BE) of 368 eV, a 90° take-off angle and the density of Au (19.3 g cm^{-3}), XPS has an information depth of 4.6 nm,[38] *i.e.* it measures the properties of the skin layer. The respective XPS spectra show an Au 4f$_{7/2}$ signal at a BE of 83.9 eV and an O 1s signal. The latter contains a component at 530.0 eV (Ag$_2$O). This signal overlaps with contributions from organic contamination typically found in liquid-processed samples. Therefore, we concentrate the discussion on the Ag 3d$_{5/2}$ signal of the residual Ag (Fig. 2). From the different values of x_{Ag} obtained by EDX (bulk), XPS (surface) and ICP-OES (entire sample) we conclude a Ag concentration gradient with higher values at the sample surface than in the bulk. The deconvolution of different Ag binding states with a small chemical shift is only sensible when the spectra were

recorded with a small pass energy of 10 eV. In order to obtain a sufficient signal-to-noise ratio, Ag concentrations above 5 at% are required that are found in the skin layer. Quantification of the different Ag binding states in the bulk of the NPG samples would require larger pass energies that cannot provide the required spectral resolution. Consequently, a quantitative determination of all Ag species by a measurement of the surface is more reliable than by a measurement in the bulk.

As shown in Fig. 2 the Ag 3d$_{5/2}$ signal contains two or three components. The component at 368.0 eV BE is caused by Ag(0). This signal is shifted by −0.2 eV against Ag(0) of a clean and pure Ag sample (indicated by the left vertical line in Fig. 2) due to the influence of the surrounding Au matrix. A plot of the Ag(0) BE in binary Au–Ag alloys at various compositions (ESI†) allows a rough estimation of the alloy composition from the Ag 3d$_{5/2}$ BE. At 368.0 eV the local Ag concentration in Au is 50 at%. Please note, the Ag 3d$_{5/2}$ lines are typi-

cally narrow and sharp so that the BE can be determined with high accuracy. All NPG samples contain a second component at 367.5 eV, *i.e.* shifted by −0.5 eV *vs.* Ag(0) in the alloy. This shift is identical to the shift of Ag_2O (indicated by the right vertical line in Fig. 2) *vs.* Ag(0) on pure Ag. This peak is thus assigned to Ag_2O at the surface of the alloy with essentially the same local composition as present for Ag(0) in the alloy. These two peaks are not sufficient to describe the Ag $3d_{5/2}$ peak of sample NPG-C so we used a third component at 367.7 eV. This BE is outside the range of Ag(0) BEs (368.2 to 367.8 eV, ESI†) in alloys of different compositions. It is thus assigned to a Ag(I) species. The higher BE than Ag_2O indicates a higher local Ag concentration because the binding energy has a shift of −0.5 eV *vs.* the Ag(0) peak of pure Ag at 368.2 eV. Please note that the peak fit is an approximation. In fact, we can expect a continuum of alloy composition after dealloying and further electrochemical treatment. The existence of the component in various intensities indicates the possibility that segregated Ag may be oxidized and remains present at the surface with a much higher local x_{Ag} than indicated by the average residual Ag content in Table 1. For brevity we call this component segregated $Ag(I)_{seg}$. XPS quantities of the different Ag components are summarized in Fig. 3.

$Ag_{50}Au_{50}$ features a significantly higher Ag concentration than obtained by XPS (Fig. 3). Thus, we conclude on a heterogeneous distribution of the Ag(0) as $Ag_{50}Au_{50}$ alloy at the surface of the sample, *e.g.* in the form of clusters as recently found.[16,31] Following this logic we conclude the presence of clusters in all NPG types investigated. Most clusters occur in samples NPG-A and NPG-B.

Irrespective of its different appearance, the presence of an Ag_2O species cannot be explained by the conditions during dealloying in strongly acidic media where Ag_2O should immediately dissolve under both, applied potential or free cor-

rosion conditions. On the other hand, the surface diffusion of Au can lead to the passivation of Ag.[39] If we take the information depth of XPS into account, a passivation of near surface-located Ag_2O by Au can be concluded to be a possible event during dealloying. In the sample state after dealloying the amount of this sub-surface Ag_2O depends only little on the dealloying route – it is highest for NPG-C and lowest for NPG-B. While its presence was shown theoretically,[40] we regard our results as the first experimental evidence for dealloying-induced sub-surface Ag_2O that had been discussed as a characteristic of as-dealloyed NPG that cannot be re-generated once it was destroyed, *e.g.* by electrochemical cycling.[41]

2.2   The influences of NPG on MEO

All MEO investigations in this study were performed in an alkaline environment. Fig. 4 compares the CVs in 1 M KOH with the CH_3OH-containing electrolyte on a planar Au electrode. In the CH_3OH-free electrolyte a current plateau at approximately 400 mV (denoted as A1, peak current density: I_P/A = 18 µA cm^{-2}) is attributed to hydroxide (Au–OH) formation (Fig. 4).[42] The cathodic scan shows a peak at 120 mV (C1) attributed to the hydroxide stripping reaction, besides another current increase towards the lower scan limit.

The CV of the CH_3OH-containing electrolyte shows significant differences: (i) a broad peak at 283 mV (with I_P/A = 74 µA cm^{-2}, denoted as AM1) that is attributed to the four-electron oxidation of CH_3OH to $HCOO^-$ [23] and that overlaps with the A1 signal, (ii) an additional anodic peak in the negative going scan (at ≈60 mV, denoted as AM2) that overlaps with C1. On planar Au electrodes AM2 had been attributed[43] to the same four-electron reaction as responsible for AM1.[23] Although this must not necessarily hold for porous electrodes, we further
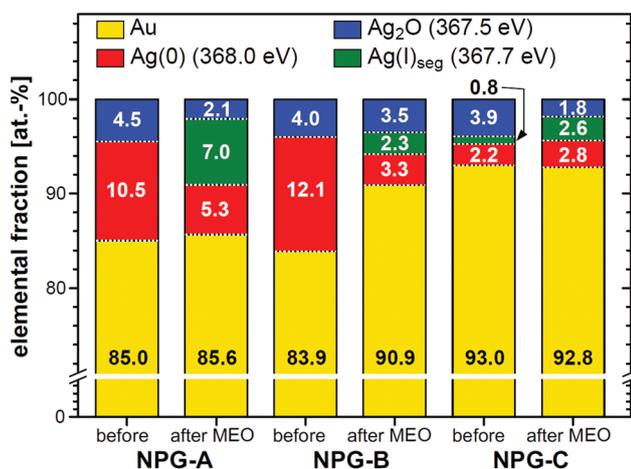

Fig. 3 Composition of differently prepared NPG electrodes before and after 10 cycles of MEO regarding exclusively Au and Ag XPS signals. Different Ag components were obtained by the deconvolution of the Ag $3d_{5/2}$ peaks. Numbers refer to the fractions of the peaks to the summed integral of all Ag and Au peaks.
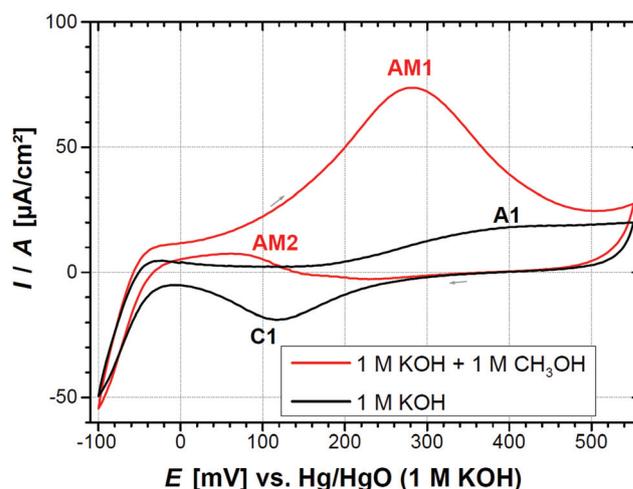

Fig. 4 Cyclic voltammogram of planar Au in 1 M KOH with (red) and without 1 M CH_3OH (black). Current (*I*) is normalized to the electrochemical active surface area (*A* = 5.2 cm^2). See the text for the peak assignment in the figure. Grey arrows indicate scan direction. Scan rate: 10 mV s^{-1}.

focus our discussion on the AM1 peak which is less distorted by the overlap with A1 than AM2 with CM1.

MEO on porous electrodes was conducted under identical conditions as for planar electrodes (Fig. 5). Cycling in the CH_3OH-free electrolyte shows small differences among the three types of NPGs tested. During cathodic scans the C1 peak current densities I_P/A decrease going from NPG-A to NPG-C.

Cycling in the CH_3OH-containing electrolyte reveals significant differences between both, the three different types of NPG as well as among NPG and planar Au. Irrespective of the scan number, the I_P of AM1 increases in the order NPG-A < planar Au < NPG-B < NPG-C (Table 1). The obtained activities (i.e. peak currents of AM1 I_P related to the active surface area A) of 42 μA cm^{-2} (NPG-A), 101 μA cm^{-2} (NPG-B) and 127 μA cm^{-2} (NPG-C) (Table 1) are within the range or slightly higher than previously reported values for NPG electrodes of different format. Xu et al.[27] reported a current density of 22 μA cm^{-2} for methanol oxidation. Other studies are only comparable with some caution. Xia et al.[28] stated a current density 50 μA cm^{-2} for aggregated gold nanoparticles. Zhang et al.[20] obtained 87 μA cm^{-2} for NPG made from a master alloy with significantly lower Ag content (42 at%) than in our study. They also used a different method for the determination of A which may have an influence on the obtained activity. Pedireddy et al.[26] reported values for open porous gold micro-bowls of 130–200 μA cm^{-2}, but these were obtained under an increased scan rate in the CV that crucially affects the obtained current densities. Similarly, NPG modified with titania nanoparticles were characterized for MEO by Kudo et al.[44] with a tenfold increased scan rate and resulted in I_P/A = 80 μA cm^{-2}, a value that is not higher than ours due to the larger scan rate used.

However, NPG-A has the largest surface and the smallest pores of all types. Ligaments with small L_B feature a higher curvature[45] and consequently more low-coordinated atoms per surface area than coarser NPG. Low coordinated sites are typically associated with higher activity,[46] but the sample with the highest number of those sites shows the lowest current density. Apart from the active site distribution, the observed activity scaling is more consistent with the explanation that an inefficient methanol saturation inside the nanopores, i.e. transport control, is most likely to occur within the smallest pores so that increased activity is present for coarser structures because they suffer less from transport control. Among the three NPG types tested, the coarsest (NPG-B and C) even exceed the activity of planar Au. Furthermore, past investigations concluded on the activity-promoting effects of Ag residues in NPG towards gas phase catalysis.[18] While Ag was found to structurally stabilize NPG towards electro-catalytic processes,[47] we did not find a clear correlation between x_{Ag} and the respective electro-oxidation activity. However, compared with the literature, all activity values exceed the reported values of Ag-free porous Au electrodes, e.g. by Xu et al.[27] or Xia et al.[28]

During ten scans we observe a slight decay of I_P for the AM1 peak (NPG-A: −8.5%, NPG-B: −8.7%, NPG-C: −8.0%) and a shift of the peak potential E_P towards less positive potentials while they are higher than for planar Au. Additionally, AM1 peaks are significantly broadened with peaks narrowing from NPG-A (full peak width at half maximum [FWHM] 565 mV) to NPG-B (FWHM: 442 mV) to NPG-C (FWHM: 356 mV) compared to planar Au (FWHM: 250 mV). We suspect this peak to consist of the overlapping signals of three contributing reactions: (i) OH adsorption on Au which was identified as a process necessary for the oxidation of alcohols.[48] (ii) The two-electron oxidation of CH_3OH to HCHO which takes place at a lower standard potential (at +166 mV vs. Hg/HgO, as calculated from ref. 49) than (iii) the four-electron reaction of CH_3OH to HCOO$^-$ that occurs at +390 mV vs. Hg/HgO[50] so that we assume that currents occurring due to the latter reaction are responsible for broadening the peak in the direction of more positive potentials compared to the case when only two electrons are transferred. Changes of the peak shape and height can be indicative of a shifted balance between these reactions, i.e. a different product selectivity (see the discussion below).
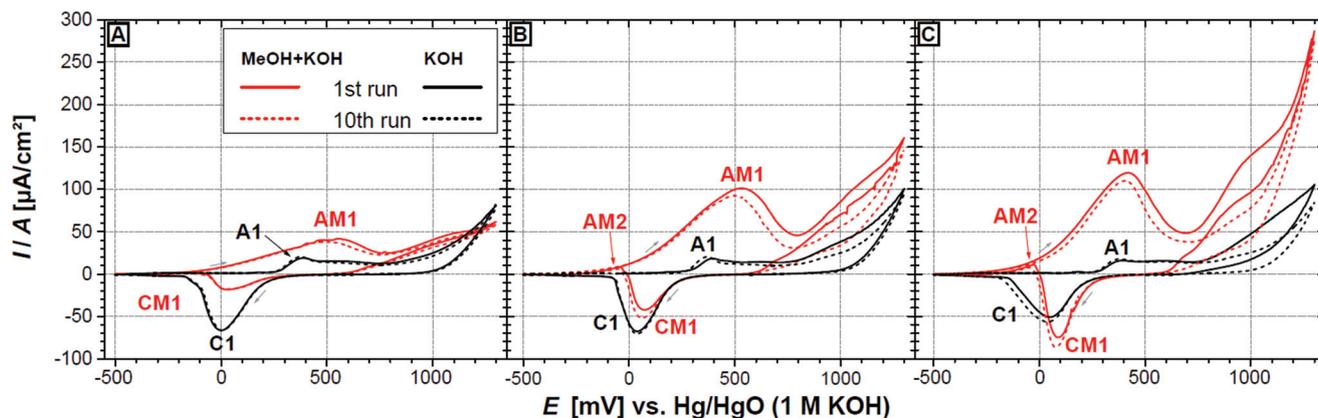

Fig. 5 Cyclic voltammograms for NPG samples in 1 M KOH (black) and 1 M KOH + 1 M CH_3OH (red). CVs in A−C were recorded for NPG resulting from different dealloying routes A−C. Currents (*I*) are normalized to the electrochemically active surface area *A*. See the text for the peak assignment in the figure. Grey arrows indicate scan direction. Scan rate: 10 mV s^{-1}.

The third observation entails the presence of a CM1 peak that increases in the order NPG-A < NPG-B < NPG-C and underlies a further increase with the scan number for NPG-B and NPG-C. Furthermore, CM1 overlaps with the C1 peak. An AM2 peak is perceptible only in cases of NPG-B and NPG-C.

To shed more light on the transport control we recorded current transients during chronoamperometry (CA) measurements (Fig. 6) applying the respective E_P of each electrode obtained by CV measurements (see Table 1). Currents under normalization to the respective value of A are shown in Fig. 6A, in which planar Au represents the most active electrode for methanol conversion followed by NPG-C, NPG-A and NPG-B. While planar Au maintains a relatively stable current over the entire duration of 600 s, the currents at the NPG electrodes drop faster. Vertical dashed lines in Fig. 6 indicate the time t_Q after which a faradaic charge was transferred that corresponds to the four-electron oxidation of the CH_3OH that is initially contained in the pore volume (as calculated from the initial sample volume by subtraction of the Ag volume and correcting

for sample shrinkage) before the electrolysis. This amount is converted fastest in the case of NPG-A and slowest in the case of NPG-B. This is reflected by a change of the slope dI/dt which coincides with t_Q in the case of NPG-B, i.e. after the methanol content in the pores is exhausted. Consequently, the observed current drop originates from the transport limitation that occurs when CH_3OH is transported from the solution bulk into the porous electrode. From the parallelism of the decay curves we conclude that this limitation affects all electrodes independently of the pore size (which scales with L_B). Furthermore, samples that were observed to show a skin with finer ligaments at the surface (NPG-A and NPG-B) show less activity than the sample without such a skin (NPG-C). Smaller pores in the skin can consequently be treated as an origin for additional diffusion limitation towards reactant molecules. On the other hand, the smaller ligaments (with higher surface-to-volume ratio) in the skin contribute more to the total surface area. A coarse estimation of the ratio of the skin surface area to A gives a value ≈1% (for both, NPG-A and NPG-B). Because this ratio of the skin is significantly less than the differences in activity compared to NPG-C (no skin), a differentiation of the activity between skin and bulk ligaments cannot be justified.

Upon normalization of I on the geometric area A_{geom} (see Fig. 6B), we derive a measure for the current efficiency η of NPG towards MEO:

$$\eta = \frac{I}{A_{geom}}$$

Contrary to the activity, η of NPG is significantly higher than that of planar Au due to the increased surface-to-volume ratio. Consequently, NPG-A shows the most outstanding current efficiency compared to the coarser NPG types. Compared to planar Au we find an enhancement by a factor of 250 during $t \leq t_Q$. For $t > t_Q$, η reaches a stable plateau which still exceeds the value of planar Au by one order of magnitude.

2.3 Reaction products

The AM1 peaks in Fig. 4 and 5 cover wider potential ranges than the one observed for the four-electron oxidation from CH_3OH to $HCOO^-$. As indicated above and besides capacitive charging, charges are also generated due to the formation of surface oxides/hydroxide and the two-electron-oxidation to HCHO. Since FWHMs of e.g. the AM1 peaks differ due to more than one contributing reactions, charges cannot directly be related to a certain product. Selectivity values are therefore expressed based on the absolute amounts of species found inside the electrolyte after cycling in defined potential ranges for all porous electrodes (see Fig. 7A) rather than based on charges.

The results of quantitative electrolyte analysis (Table 1) support the interpretation of a shifted MEO product selectivity (i.e. the ratio between the amount of formate to the summed amount of formaldehyde and formate) as outlined above. In contrast to planar Au, $HCOO^-$ (by ion-exchange chromatography, IEC) is the main oxidation product of CH_3OH for all
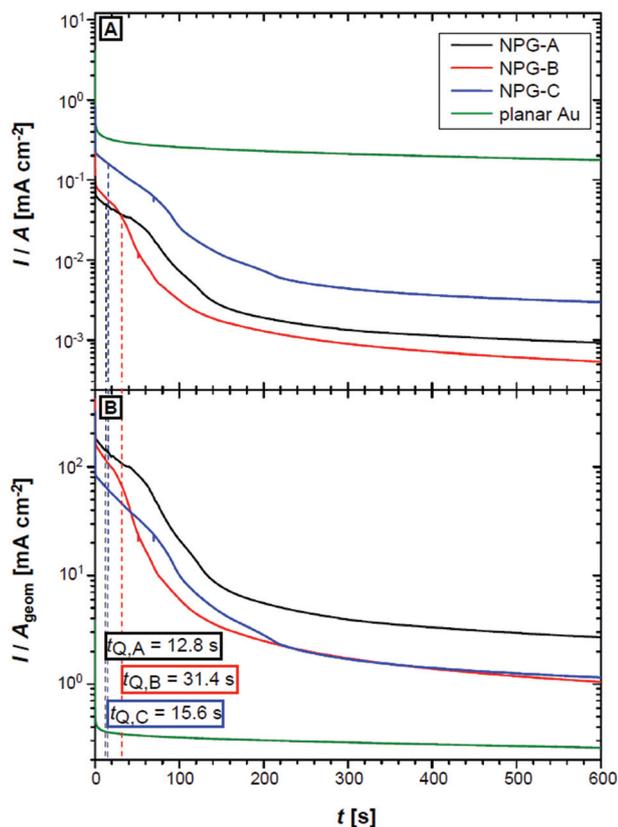
Fig. 6 Current transients as recorded for different types of NPG (see the text for details) and planar Au during chronoamperometric scans in 1 M KOH + 1 M CH_3OH. (A) Currents normalized to the electrochemical active surface area (A) of the samples. (B) Currents normalized to the geometric surface area (A_{geom}) of the samples. Applied potentials correspond to the peak potentials in Fig. 4 and 5: 550 mV (NPG-A), 510 mV (NPG-B), 410 mV (NPG-C) and 280 mV (planar Au). Vertical dashed lines indicate the times t_Q at which the amount of CH_3OH contained in the pore volume is consumed.
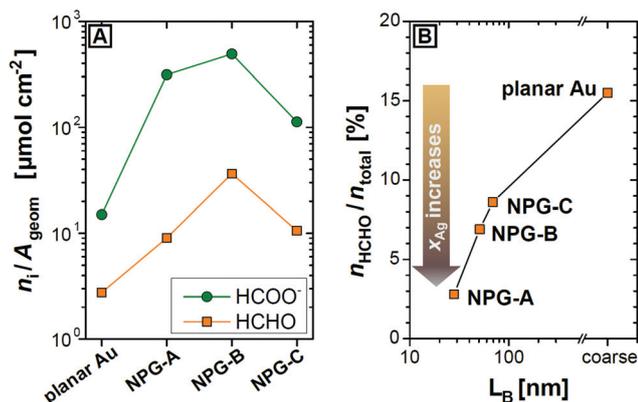
Fig. 7 Oxidation yield (A) and selectivity (B) of different types of NPG electrodes compared to planar Au towards methanol electro-oxidation during CV. (A) Amounts n_i of i = HCHO and i = HCOO⁻ per geometrical surface area A_{geom} as determined by electrolyte chromatography after cycling. (B) Fraction of HCHO on the total product amount (HCHO + HCOO⁻) in dependence on the bulk ligament size, L_B. The corresponding increase of x_{Ag} (from EDX and XPS after cycling) is indicated by the arrow.

types of NPG during cycling (Table 1). Zhang *et al.*[20] assumed the six-electron reaction to CO_3^{2-} as the only reaction occurring during MEO on NPG electrodes. Parallel to the HCOO⁻ quantification, IEC enabled the quantification of the total inorganic carbon (TIC) content which is the sum of the concentrations of CO_3^{2-} and HCO_3^-, *i.e.* the products of the six-electron oxidation reaction. We observed no changes in the TIC content (the TIC content was ≠0 due to the eluent's composition in IEC) by cycling both, planar and NPG electrodes in a CH_3OH-containing electrolyte and conclude that the six-electron reaction is not significant within the screened potential window.

Further, the HCHO concentration (by HPLC) increased slightly (its background concentration was 10 M). The HCHO fraction of the total reaction products increases in the order NPG-A < NPG-B < NPG-C < planar Au which is also reflected when displaying the oxidation yield, *i.e.* the amounts of HCHO normalized to A_{geom} (Fig. 7A). Upon normalization to A (not shown), the three types of NPG electrodes generate HCHO and HCOO⁻ amounts that are smaller than for planar Au; both amounts scale in the order A < C < B. In other words, NPG electrodes promote the four-electron reaction to HCOO⁻ and suppress the two-electron reaction. The selectivity for HCOO⁻ formation is found to be the highest for electrodes with highest x_{Ag} (Fig. 7B). While no investigations on the selectivity for electro-catalytic methanol oxidation using NPG electrodes have been published yet, we find our results in accordance with past reports on gas-phase oxidative coupling of methanol using NPG catalysts.[9] These concluded a nearly selective formation of methyl formate (the condensation product of the two-electron oxidation product HCHO with methoxy groups) when using catalysts with a low x_{Ag}. Additionally, the authors find preference for higher oxidized products (namely CO_2) when x_{Ag} is increased. Neglecting that we do not find carbon-

ate as a product, the conclusion that the oxophilic nature of Ag leads to more O adsorbates (which are regarded as the oxidant species and hence favor total oxidation when concentrated sufficiently high) is only partially applicable to our present case: upon potential increase the surface is decorated with O adsorbates mostly due to the applied potential and is relatively independent of x_{Ag}. We conclude that different selectivities are thus not directly connected to different contents of the residual Ag, but more to differences in transport, so that the selectivity is only indirectly reflected by the corresponding x_{Ag} values. Electrolyte transport is connected to the size of the pores which (due to the bi-continuity of the NPG structure[37,51,52]) is connected to the ligament size. As shown previously, x_{Ag} and L_B are interrelated,[29] such that smaller ligaments contain more Ag. Consequently, more retained Ag results in an increased transport limitation so that the fast interfacial reaction, *i.e.* the two electron oxidation to HCHO,[49] is more strongly affected than the slower four-electron oxidation to HCOO⁻. Furthermore, follow-up reactions of dissolved products (HCHO to HCOO⁻) are promoted if the initial product (here HCHO) is confined in a porous electrode.
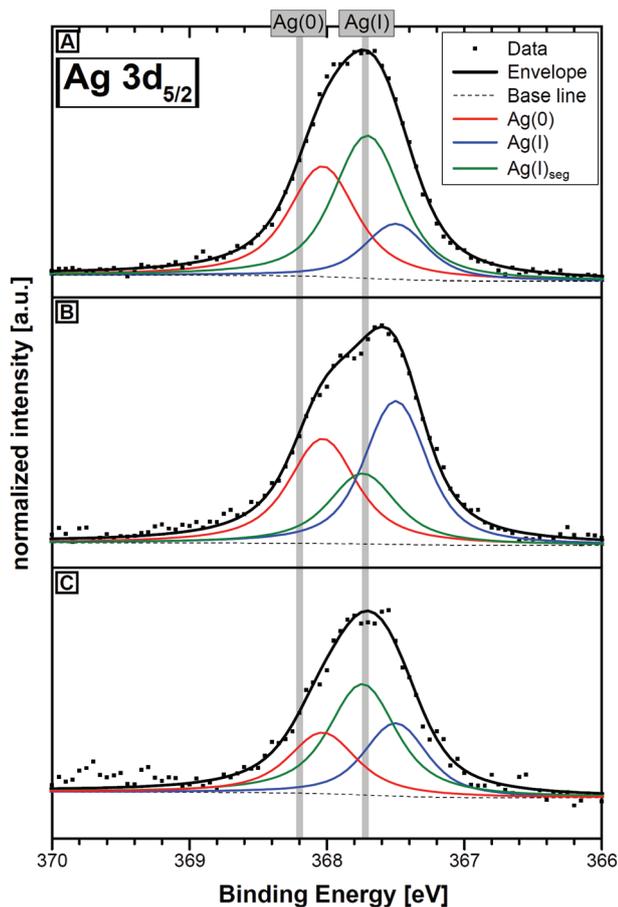
Fig. 7B displays the correlation between the HCHO content on L_B. Similar to the selectivity increase by NPG electrodes, lower amounts of HCHO correlate with decreasing L_B. A similar correlation between selectivity and x_{Ag} is also indicated in the figure. Upon regarding the true Ag contents determined after cycling we find that the higher selectivity also correlates with higher x_{Ag}.

2.4 Changes in NPG caused by MEO

Catalysis-induced ligament coarsening along with a starting clustering of the residual Ag had been identified as reasons for weakening the activity of NPG towards catalytic CO oxidation.[53] As described above, coarser ligaments expose fewer low-coordinated surface atoms resulting in a lower activity of the catalyst. During MEO CV scans and irrespective of L_B and x_{Ag} we observe a slight decrease in I_P over the same time. I_P drops the strongest for NPG-A (−9.6%), followed by NPG-B (−8.3%) and weakest for NPG-C (−7.4%) which is in all cases lower than the drop at planar electrodes (−14.3%). According to the SEM images in the second and fourth column of Fig. 1, MEO cycling seems to be less effective on L_B than concluded before for all types of NPG. Note, that eventual changes in L_B as implied by Table 1 need to be considered with respect to the standard error inherent to SEM-based L_B determination. In contrast, sample surfaces are found to coarsen significantly for samples NPG-A (L_B increases by a factor 2) and NPG-B (L_B increases by a factor 3).

Concerning the sample composition, x_{Ag} in the bulk (by EDX) does not change significantly during MEO cycling. Eventual changes are assigned to quantification errors of EDX when applied to unpolished surfaces. XPS reveals that the BEs of both, Au 4f and O 1s, did not change upon MEO cycling. In contrast, Ag $3d_{5/2}$ XPS signals (Fig. 8) change. Their analysis confirms a constant total Ag content (Table 1) except for the sample NPG-B where a decrease of x_{Ag} by approximately 31%

Fig. 8 Ag 3d$_{5/2}$ XP core level spectra for NPG made under the different dealloying protocols A–C after ten repetitive MEO cycles. See caption of Fig. 2 for further details.

samples the content of the sub-surface Ag(I) decreases. However, although correlations might exist, we restrict our conclusion to the point that a direct connection between the presence of clusters and the observations on reactivity/selectivity from above cannot be identified based on these data.

3 Conclusion

NPG, as obtained by dealloying, is expected to be a promising candidate for Pt-free bulk-scale catalysts. MEO represents a well investigated and relevant reaction, to which NPG was applied in this contribution. The variation of NPG properties, namely L_B and x_{Ag} was achieved by different dealloying protocols. We could confirm by XPS that dealloying causes the residual Ag in NPG to occur in the form of Ag-rich clusters and Ag$_2$O located below the surface. From the application of the different NPG materials as electrodes for MEO and the comparison with planar Au we outline the following key observations:

(i) Coarser types of NPG have a higher activity, while all types have a higher current efficiency towards MEO than planar Au. Even for the coarsest NPG structures a transport limitation is evident.

(ii) Compared with planar Au, NPG shows an increased selectivity for the four-electron oxidation of CH$_3$OH that can further be increased by decreasing L_B.

(iii) The internal (bulk) structure of NPG does not change during MEO while finer (surface) ligaments coarsen.

(iv) During electrocatalytic cycling, the changes in the nature of the Ag components are sensitive to the preceding dealloying protocol. Ag-rich clusters obtained by potentiostatic dealloying remain and become oxide-decorated. Sub-surface Ag$_2$O content is reduced in all cases.

While the nature of Ag has no direct implication on the MEO process itself, it is important to note that Ag generally plays a crucial role for the electro-oxidation process. The correlation between higher current activity/improved selectivity and the ligament size is shown, yet a similar correlation to the Ag content exists due to the correlation between L_B and x_{Ag} which is less obvious due to the concentration heterogeneity of Ag. On the other hand finer ligaments require higher Ag content so that the dependence on x_{Ag} can be indirect. Further investigations should focus on the nature of the high-energy Ag(I) XPS signal, a local analysis of the Ag content along the cross-section of macroscopic NPG samples, a long-term screening of the MEO current efficiency and an increase of the Ag content to achieve enhanced selectivities besides finer and more stable ligaments.

4 Experimental part

4.1 Electrode preparation and characterization

Au and Ag, at the ratio Au$_{28}$Ag$_{72}$ (subscripts: at%), were alloyed by arc-melting, sealed under Ar in fused silica and annealed

is found. In the alkaline environment Ag$_2$O is insoluble, *i.e.* a Ag dissolution can be excluded. Simultaneously, NPG-B shows the strongest coarsening of the surface so that the loss of Ag(0) can be attributed to the diffusion of Au that buries Ag deeper than the XPS information depth. The deconvolution of the Ag 3d$_{5/2}$ peaks reveals the same components as before cycling, *i.e.* Ag(0) at 368.0 eV and Ag(I) at 367.5 eV. The third component (Ag(I)$_{seg}$ at 367.7 eV) which was initially present only in sample NPG-C is now present in all three samples. In the case of NPG-A, Ag(I)$_{seg}$ evolves partly from Ag(0), and partly from the sub-surface Ag(I) due to its exposure by Au surface diffusion. As outlined above and confirmed before,[16,31] NPG-A and NPG-B also featured Ag-rich clusters before catalysis. We conclude for the case NPG-A that these clusters oxidize to Ag$_2$O (represented by the Ag(I)$_{seg}$ fraction). Only a smaller fraction of the sub-surface Ag$_2$O contributes to this oxide. In the case of NPG-B, the Ag(0) fraction that was not passivated remains as clusters that are covered in the same way. In the case of NPG-C where clusters occur because of the low total Ag concentration, the sub-surface Ag$_2$O is dominantly converted into the Ag(I)$_{seg}$ species while the Ag(0) content slightly increases possibly as a result of an ongoing clustering which is accompanied by its oxide coverage. In all

for 5 d at 925 °C for homogenization. The alloy ingots were cold-rolled to a 150 m thick foil and laser-cut to circular disc samples of 5 mm diameter.

Dealloying was carried out *via* three different routes as described earlier.[29] Briefly, samples denoted as NPG-A were produced by potentiostatic dealloying using a Metrohm Autolab PGStat10 potentiostat in 1 M HClO₄ according to Parida *et al.*[54] using a coiled Ag wire as a counter electrode (CE) and a Ag/AgCl reference electrode (RE) under a stepped dealloying potential regime (24 h at 1050 mV, 8 h at 1100 mV, 8 h at 1150 mV and 10 h at 1200 mV *vs.* Ag/AgCl) to avoid stress-corrosion cracking. Samples denoted as NPG-B were produced by potentiostatic dealloying according to Wittstock *et al.*[55] in 5 M HNO₃ against a Pt foil as CE and a Pt pseudo-RE under a constant dealloying potential of 60 mV *vs.* Pt for 24 h. Samples denoted as NPG-C were produced by dealloying under open-circuit conditions according to Rouya *et al.*,[34] *i.e.* by immersion into 7.25 M HNO₃ thermostated at 65 °C for 24 h.

After dealloying, all samples were washed in de-ionized water, cleaved carefully into two halves and stored under fresh water. One half of the cleaved NPG sample was further used for MEO experiments while the other remained under water. Investigations on planar Au were performed on a coiled Au wire with 50 m diameter and 2.73 m length.

Prior to MEO investigations, we applied the capacitance ratio method in order to determine A of the porous and planar samples.[32] Samples were immersed into 0.1 M HClO₄. CV scans were made with a Hg/Hg₂SO₄ RE and carbon cloth CE within a range of ±50 mV around the open-circuit potential (OCP = 520 (NPG-A)-120 (NPG-C) mV *vs.* Hg/Hg₂SO₄) at scan rates v of 1, 3, and 5 mV s⁻¹. To obtain A, the net capacity was compared to the specific capacitance of a non-oxidized Au surface (40 µF cm⁻²) at the applied potential.[33]

All nanoporous samples were investigated by scanning electron microscopy (SEM) using a Leo Gemini 1530 microscope in cross-sectional and top-view. Ligament sizes were derived from SEM micrographs at 250 000× magnification by averaging 20 diameters. EDX spectra were recorded from 20 µm × 30 µm areas in cross-view to determine the residual Ag content in bulk NPG, x_{Ag-EDX}.

XPS was performed using an ESCALAB 250 Xi instrument (Thermo Fisher) with mono-chromatized Al K$_\alpha$ ($h\nu$ = 1486.6 eV) radiation. All samples (sample halves before and after MEO) were dried and stored under Ar. High resolution spectra were measured with a pass energy of 10 eV. Peak deconvolution was performed using a Gaussian–Lorentzian peak shape by the software Avantage (Thermo Fisher).

4.2 Methanol electro-oxidation

After the determination of A, the sample was subsequently washed in de-ionized water and immersed into a N₂-flushed 1 M KOH + 1 M CH₃OH solution. The soaked NPG samples were transferred into a three-neck flask filled with 50 ml of the degassed 1 M KOH + 1 M CH₃OH solution, Au wire CE and Hg/HgO RE under constant N₂ flushing until a stable OCP of −440 mV *vs.* Hg/HgO was reached. MEO cycling was then per-

formed from −440 mV to 1300 mV at v = 10 mV s⁻¹ for ten successive cycles. After cycling, 40 ml of the electrolyte were transferred to quantitative analysis. The NPG sample was cleaned in de-ionized water. CV scans in CH₃OH-free 1 M KOH were performed at separately prepared NPG samples using equivalent procedures of cleaning, A determination and cycling. During CA scans in 1 M KOH + 1 M CH₃OH electrolytes the found peak potentials were applied for 10 min in the same setup with separately prepared NPG samples.

4.3 Quantitative analysis

HCHO quantification was performed by using HPLC using an Agilent HPLC Infinity equipped with an Ultrasphere 5μ column. After neutralization of the alkaline electrolyte solutions with H₃PO₄, HCHO was derivatized based on Brady's test[56] using 100 µl of a 21 mM solution of 2,4-dinitrophenylhydrazine (DNPH) in H₃PO₄ and mixing it with 1 ml electrolyte solution and 8 ml acetonitrile for 3 h. After centrifugation the supernatant HCHO-DNPH derivative was quantified by using HPLC at 40 °C using an eluent mixture of 1 : 1 (v/v) water : acetonitrile at a flow rate of 1 ml min⁻¹ and UV-Vis detection at 360 nm. Quantitative analysis of the initial electrolyte (1 M KOH + 1 M CH₃OH) gave a HCHO concentration of 10 µM as the background value.

HCOO⁻ quantification was achieved by using IEC using an ICS 1100 System from Thermo Fisher Scientific equipped with a 4 × 50 mm pre-column (Dionex AG22) and a 250 × 4 mm main column (Dionex AS22). 25 µl of the electrolyte were injected at room temperature into the system using a 5 mM Na₂CO₃ + 1.25 mM NaHCO₃ aqueous eluent solution at a flow rate of 1 ml min⁻¹ and detection *via* electrical conductivity. HCOO⁻ and TIC quantification was achieved after calibration within a CH₃OH-free matrix. The initial electrolyte contained no detectable HCOO⁻.

Conflicts of interest

There are no conflicts to declare.

Acknowledgements

References

1 D. Kramer, R. N. Viswanath and J. Weissmüller, *Nano Lett.*, 2004, **4**, 793–796.
2 L. Zhang, L. Chen, H. Liu, Y. Hou, A. Hirata, T. Fujita and M. Chen, *J. Phys. Chem. C*, 2011, **115**, 19583–19587.
3 E. Detsi, Z. G. Chen, W. P. Vellinga, P. R. Onck and J. T. M. De Hosson, *J. Nanosci. Nanotechnol.*, 2012, **12**, 4951–4955.
4 C. Stenner, L.-H. Shao, N. Mameka and J. Weissmüller, *Adv. Funct. Mater.*, 2016, **26**, 5174–5181.

5   D. Jalas, L.-H. Shao, R. Canchi, T. Okuma, S. Lang, A. Petrov, J. Weissmüller and M. Eich, *Sci. Rep.*, 2017, **7**, 44139.

6   X. Y. Lang, H. T. Yuan, Y. Iwasa and M. W. Chen, *Scr. Mater.*, 2011, **64**, 923–926.

7   D. Li, Y. Zhu, H. Wang and Y. Ding, *Sci. Rep.*, 2013, **3**, 3015.

8   A. Wittstock, A. Wichmann and M. Bäumer, *ACS Catal.*, 2012, **2**, 2199–2215.

9   A. Wittstock, V. Zielasek, J. Biener, C. M. Friend and M. Bäumer, *Science*, 2010, **327**, 319–322.

10 R. Li and K. Sieradzki, *Phys. Rev. Lett.*, 1992, **68**, 1168–1171.

11 A. Pareek, S. Borodin, A. Bashir, G. N. Ankah, P. Keil, G. A. Eckstein, M. Rohwerder, M. Stratmann, Y. Gründer and F. U. Renner, *J. Am. Chem. Soc.*, 2011, **133**, 18264–18271.

12 X. Wang, J. Frenzel, W. Wang, H. Ji, Z. Qi, Z. Zhang and G. Eggeler, *J. Phys. Chem. C*, 2011, **115**, 4456–4465.

13 N. Asao, Y. Ishikawa, N. Hatakeyama, Menggenbateer, Y. Yamamoto, M. Chen, W. Zhang and A. Inoue, *Angew. Chem., Int. Ed.*, 2010, **49**, 10093–10095.

14 J. K. Nørskov, T. Bligaard, A. Logadottir, J. R. Kitchin, J. G. Chen, S. Pandelov and U. Stimming, *J. Electrochem. Soc.*, 2005, **152**, J23–J26.

15 Y.-C. K. Chen-Wiegart, R. Harder, D. Dunand and I. McNulty, *Nanoscale*, 2017, **9**, 5686–5693.

16 C. Mahr, P. Kundu, A. Lackmann, D. Zanaga, K. Thiel, M. Schowalter, M. Schwan, S. Bals, A. Wittstock and A. Rosenauer, *J. Catal.*, 2017, **352**, 52–58.

17 T. Fujita, P. Guan, K. McKenna, X. Lang, A. Hirata, L. Zhang, T. Tokunaga, S. Arai, Y. Yamamoto, N. Tanaka, Y. Ishikawa, N. Asao, Y. Yamamoto, J. Erlebacher and M. Chen, *Nat. Mater.*, 2012, **11**, 775–780.

18 L. V. Moskaleva, S. Röhe, A. Wittstock, V. Zielasek, T. Klüner, K. M. Neyman and M. Bäumer, *Phys. Chem. Chem. Phys.*, 2011, **13**, 4529–4539.

19 M. M. Montemore, R. J. Madix and E. Kaxiras, *J. Phys. Chem. C*, 2016, **120**, 16636–16640.

20 J. Zhang, P. Liu, H. Ma and Y. Ding, *J. Phys. Chem. C*, 2007, **111**, 10382–10388.

21 Y. E. Seidel, A. Schneider, Z. Jusys, B. Wickman, B. Kasemo and R. J. Behm, *Langmuir*, 2010, **26**, 3569–3578.

22 H. Wang, C. Wingender, H. Baltruschat, M. Lopez and M. T. Reetz, *J. Electroanal. Chem.*, 2001, **509**, 163–169.

23 Z. Borkowska, A. Tymosiak-Zielinska and G. Shul, *Electrochim. Acta*, 2004, **49**, 1209–1220.

24 G. Tremiliosi-Filho, E. R. Gonzalez, A. J. Motheo, E. M. Belgsir and J. Le, *J. Electroanal. Chem.*, 1998, **444**, 31–39.

25 H. Wang, L. Zhu, L. Yang, F. Liao, M. Sheng, B. Jiang and M. Shao, *Mater. Chem. Phys.*, 2017, **186**, 301–304.

26 S. Pedireddy, H. K. Lee, C. S. L. Koh, J. M. R. Tan, W. W. Tjiu and X. Y. Ling, *Small*, 2016, 4531–4540.

27 Y. Xu, X. Ke, C. Yu, S. Liu, J. Zhao, G. Cui, D. Higgins, Z. Chen, Q. Li and G. Wu, *Nanotechnology*, 2014, **25**, 445602–445608.

28 H. Xia, Y. Ran, H. Li, X. Tao and D. Wang, *J. Mater. Chem. A*, 2013, **1**, 4678–4684.

29 M. Graf, B. Roschning and J. Weissmüller, *J. Electrochem. Soc.*, 2017, **164**, C194–C200.

30 S. Cattarin, D. Kramer, A. Lui and M. M. Musiani, *J. Phys. Chem. C*, 2007, **111**, 12643–12649.

31 T. Krekeler, A. V. Straßer, M. Graf, K. Wang, C. Hartig, M. Ritter and J. Weissmüller, *Mater. Res. Lett.*, 2017, **3831**, 314–321.

32 S. Trasatti and O. Petrii, *Pure Appl. Chem.*, 1991, **63**, 711–734.

33 P. S. Germain, W. G. Pell and B. E. Conway, *Electrochim. Acta*, 2004, **49**, 1775–1788.

34 E. Rouya, S. Cattarin, M. L. Reed, R. G. Kelly and G. Zangari, *J. Electrochem. Soc.*, 2012, **159**, K97–K102.

35 J. Biener, A. Wittstock, L. A. Zepeda-Ruiz, M. M. Biener, V. Zielasek, D. Kramer, R. N. Viswanath, J. Weissmüller, M. Bäumer and A. V. Hamza, *Nat. Mater.*, 2009, **8**, 47–51.

36 L. C. Wang, Y. Zhong, H. Jin, D. Widmann, J. Weissmüller and R. J. Behm, *Beilstein J. Nanotechnol.*, 2013, **4**, 111–128.

37 X. L. Ye, N. Lu, X. J. Li, K. Du, J. Tan and H. J. Jin, *J. Electrochem. Soc.*, 2014, **161**, 517–526.

38 S. Tanuma, C. J. Powell and D. R. Penn, *Surf. Interface Anal.*, 2011, **243**, 689–713.

39 K. Sieradzki, N. Dimitrov, D. Movrin, C. McCall, N. Vasiljevic and J. Erlebacher, *J. Electrochem. Soc.*, 2002, **149**, B370–B377.

40 S. Hoppe, Y. Li, L. V. Moskaleva and S. Muller, *Phys. Chem. Chem. Phys.*, 2017, **22**, 14845–14853.

41 H. J. Jin, S. Parida, D. Kramer and J. Weissmüller, *Surf. Sci.*, 2008, **602**, 3588–3594.

42 L. D. Burke, D. T. Buckley and J. A. Morrissey, *Analyst*, 1994, **119**, 841–845.

43 K. A. Assiongbon and D. Roy, *Surf. Sci.*, 2005, **594**, 99–119.

44 A. Kudo, T. Fujita, X. Y. Lang, L. Y. Chen and M. W. Chen, *Mater. Trans.*, 2010, **51**, 1566–1569.

45 J. Weissmüller, R. C. Newman, H.-J. Jin, A. M. Hodge and J. W. Kysar, *Mater. Res. Soc. Bull.*, 2009, **34**, 577–586.

46 A. P. O'Mullane, *Nanoscale*, 2014, **6**, 4012–4026.

47 A. Y. Chen, J. W. Wang, Y. Wang, Y. Q. Jia, J. F. Gu, X. F. Xie and D. Pan, *Electrochim. Acta*, 2015, **153**, 552–558.

48 J. S. Spendelow and A. Wieckowski, *Phys. Chem. Chem. Phys.*, 2007, **9**, 2654–2675.

49 H. Okamoto, T. Gojuki, N. Okano, T. Kuge, M. Morita, A. Maruyama and Y. Mukouyama, *Electrochim. Acta*, 2014, **136**, 385–395.

50 W. H. Koppenol and J. D. Rush, *J. Phys. Chem.*, 1987, **91**, 4429–4430.

51 T. Fujita, L. H. Qian, K. Inoke, J. Erlebacher and M. W. Chen, *Appl. Phys. Lett.*, 2008, **92**, 90–93.

52 C. A. Volkert, E. T. Lilleodden, D. Kramer and J. Weissmüller, *Appl. Phys. Lett.*, 2006, **89**, 87–90.

53 T. Fujita, T. Tokunaga, L. Zhang, D. Li, L. Chen, S. Arai, Y. Yamamoto, A. Hirata, N. Tanaka, Y. Ding and M. Chen, *Nano Lett.*, 2014, **14**, 1172–1177.

54 S. Parida, D. Kramer, C. A. Volkert, H. Rösner, J. Erlebacher and J. Weissmüller, *Phys. Rev. Lett.*, 2006, **97**, 4–7.

55 A. Wittstock, A. Wichmann, J. Biener and M. Bäumer, *Faraday Discuss.*, 2011, **152**, 87–98.

56 O. L. Brady and G. V. Elsmie, *Analyst*, 1925, **51**, 77–78.